Contents lists available at ScienceDirect

# **Composites Part B**

journal homepage: www.elsevier.com/locate/composites





# Validation and verification of a novel higher-order FE Framework for process modeling of thermoset composites

M.H. Nagaraj <sup>a,1</sup>, S.P. Shah <sup>a,1</sup>, A. Sabato <sup>a,2</sup>, M. Maiaru <sup>b,3,\*</sup>

- <sup>a</sup> Department of Mechanical Engineering, University of Massachusetts Lowell, MA 01854, United States
- <sup>b</sup> Department of Civil Engineering and Engineering Mechanics, Columbia University, NY 10027, United States

# ARTICLE INFO

# Keywords: Process modeling CUF Higher-order structural modeling Residual stresses

#### ABSTRACT

Uncontrolled curing-induced residual stress is a significant limitation to the efficient design of thermoset composite structures, and a sufficiently high post-cure stress state can compromise their performance, durability, and geometrical tolerance. Experimentally validated multiscale process models aid in quantitatively describing the relation between process parameters and residual stress development across composite length scales, thereby allowing for an optimized manufacturing process and improved part performance. This work presents a novel numerical approach for the process modeling of fiber-reinforced thermosets, and is based on higher-order finite elements derived from the Carrera Unified Formulation. The process framework is experimentally validated at the macro-scale using cure-induced warpage data of fabricated cross-ply laminates. Micromechanical process analysis is performed to predict residual stress evolution at the micro-scale, and a comparison with reference 3D-FEA provides a verification of the proposed approach. The predicted laminate-level cure-induced warpage is found to be within 9% of experimental measurements, thereby validating the presented process model, while comparing the micromechanical analysis costs with conventional 3D-FEA demonstrates an order-of-magnitude improvement in computational efficiency. The performance of the proposed computational models constitutes a milestone towards enabling practically feasible multiscale process modeling for composites structures.

# 1. Introduction

Fiber-reinforced plastics (FRP) have become increasingly popular in many industries, including aerospace, automotive, and wind, due to their outstanding mechanical properties, such as specific strength and stiffness. However, their complex mechanical response and uncertainties in their properties due to manufacturing imperfections lead to the use of larger margins of safety and an overly conservative design, which restricts the utilization of the full potential of composite materials and limits structural efficiency. A further bottleneck is the large design space associated with composite structures, which renders physical testing a lengthy and resource-intensive task.

The manufacturing process of thermoset FRP has a significant effect on both the final geometry of the part as well as its mechanical performance. The manufacturing process, or curing, consists of an exothermic chemical reaction, during which material properties change as a function of time and temperature. The thermal expansion mismatch between fibers and matrix leads to differential expansion within the composite microstructure. Such thermal expansion mismatch at the level of the constituents, in combination with chemical shrinkage of the matrix and the thermo-mechanical properties evolution during the cure cycle, results in self-equilibrated residual stresses [1,2]. High residual stress levels during the cure cycle can lead to the formation of micro-cracks within the matrix, significantly reducing the composite mechanical performance and service life [3,4]. At the structural scale, post-cure residual stresses can cause warping of the structure, resulting in dimensional changes which can impact geometrical tolerances and hence assembly [5]. This is of particular importance in the fabrication of thin-walled composite airframe components, where process-induced distortions such as spring-in of angled parts and warpage in flat laminates can greatly increase time and labor required during the assembly phase. The robust design and optimization of composite structures thus requires an accurate understanding of the development of residual stresses within the manufactured part.

E-mail addresses: manish\_nagaraj@uml.edu (M.H. Nagaraj), sagar\_shah@uml.edu (S.P. Shah), alessandro\_sabato@uml.edu (A. Sabato), mm6263@columbia.edu (M. Maiaru).

- <sup>1</sup> Postdoctoral Research Associate
- <sup>2</sup> Assistant Professor
- <sup>3</sup> Associate Professor

<sup>\*</sup> Corresponding author.

Computationally efficient multiscale process modeling is needed to predict curing-induced residual stresses accurately [6]. Different numerical techniques can reproduce the fundamental physical phenomena across the relevant length-scales in fiber-reinforced composites, including the evolution of the mechanical and non-mechanical properties of the matrix as a function of curing, local fiber constraint of the curing matrix, thermal gradients, and stress concentrations induced by complex tow architectures [7-12]. Recent work has shown that it is possible to virtually reproduce the cross-linking formation of the polymer during curing at the nano-scale using Molecular Dynamics (MD) simulations [13,14]. MD simulations accurately represent the chemical composition of the resin and its curing agent and predict the mechanical property evolution of the matrix as a function of the crosslinking density [15-17]. The local variation in fiber volume fraction driven by the stochastic distribution of the fibers induces local variability in the residual stress state, which in turn affects the mechanical properties of the curing resin. Additionally, fiber proximity can act as a stress riser in the microstructure that triggers premature failure [18-20]. Modeling the micro-scale resolution enables the explicit representation of the reinforcing fibers and the resulting stochastic property variabilities within the composite constituents needed to represent a realistic structure [21– 231. Thus, the explicit modeling of the fibers at the micro-scale is crucial to predict the composite failure behavior accurately [24-28]. While traditional 3D Finite Element (3D-FE) analysis is a preferred tool to analyze complex structures at the macro-scale [29,30], computational micromechanical models based on conventional FE can incur prohibitively high costs, especially when they are used in a multiscale setting to inform composite material behavior in a structural-level analysis [31]. Thus, a computationally-efficient numerical approach is necessary to model the microstructure, which would eventually form part of multiscale process modeling frameworks.

Several cure models have been proposed in the literature [32-34], with one of the most popular formulations being the phenomenological model by Kamal and Sourour [35]. These kinetic models have been used in various numerical investigations on the prediction of residual stresses during the curing process, as well as the influence of these stresses on the effective mechanical properties of the composite. For instance, Ding et al. proposed a 3D thermo-viscoelastic model to simulate residual stresses in composite laminates during curing [36]. Maiaru et al. investigated the influence of the manufacturing process on the transverse strength of unidirectional FRP using traditional FEs [20]. More recently, Hui et al. developed a micro-scale viscoplastic model to investigate the effect of curing-induced stresses on the compressive strength of unidirectional FRP [37]. Similarly, D'Mello et al. presented an approach to simulate the curing process of homogenized textile composites and subsequently evaluated the effect of the developed residual stresses on the tensile strength of the composite [30].

The objective of the present work is to validate a novel computationally efficient process modeling framework based on higher-order FEs at the macro-scale (laminate-level) using cure-induced deformation data measured from fabricated cross-ply laminates. Subsequently, the performance of the proposed process model at the micro-scale is evaluated and verified using traditional 3D-FEA. The structural modeling is derived from the Carrera Unified Formulation (CUF), a generalized theoretical framework to develop higher-order structural theories, which are then implemented in the form of higher-order FEs. CUFbased models are capable of an accuracy approaching that of 3D-FE at significantly reduced computational effort [38]. The advantages of CUF have been demonstrated in recent years for various classes of problems, such as progressive damage and impact analysis [39-41], micromechanical analysis [42-44], material extrusion additive manufacturing [45], and the analysis of process-induced deformations in cured composite parts [46].

The present work is organized in the following manner: Section 2 describes the thermoset constitutive model and the higher-order structural modeling approach used in the present work. Section 3 provides

an overview of the experimental validation of the process model at the macro-scale. Section 4 consists of the process model verification at the micro-scale, via a comparison with traditional FEs, along with an evaluation of the proposed model's performance. The main conclusions are summarized in Section 5.

$$\frac{d\phi}{dt} = A \exp\left(-\frac{E_a}{RT}\right) \phi^n (1 - \phi^m) \tag{1}$$

#### 2. Higher-order FE process modeling

The proposed higher-order FE process modeling reproduces the constitutive behavior of the resin during curing. The constitutive modeling is described in Section 2.1, while the numerical approach is discussed in Section 2.2.

## 2.1. Constitutive modeling

The thermoset cure kinetics for a given cure cycle, see Fig. 1, is governed by an auto-catalytic phenomenological semi-empirical kinetic model [35], as follows

$$\frac{d\phi}{dt} = \left[ A_1 exp\left( -\frac{\Delta E_1}{RT} \right) + A_2 exp\left( -\frac{\Delta E_2}{RT} \right) \phi^n \right] (1 - \phi^m) \tag{2}$$

where  $\phi$  is the degree of cure, R is the gas constant, T is the cure temperature at time t, with the activation energies denoted by  $\Delta E_1$  and  $\Delta E_2$ . The constants  $A_1$  and  $A_2$ , and the exponents m and n, are determined experimentally. The thermal state of the thermoset is a consequence of the prescribed cure temperature and the heat generated due to the exothermic nature of the curing process, and the resulting temperature distribution is evaluated using the Fourier heat transfer model as follows

$$\rho c_p \frac{dT}{dt} = \kappa_i \frac{d^2T}{dt^2} + \frac{dq}{dt}, \text{ with } \frac{dq}{dt} = \rho H_T \frac{d\phi}{dt}$$
 (3)

where  $\rho$  and  $c_p$  are respectively the density and specific heat of the epoxy,  $\kappa_i$  is the thermal conductivity, q is the instantaneous exothermic heat generated during the curing process, and  $H_T$  is the total heat of reaction.

During the curing process, the change in the degree of cure (as a function of time) results in an evolution of the chemo-rheological and thermo-mechanical properties of the thermoset. These temperature-dependent properties have been previously characterized in-house for the RIM R135/H1366 epoxy resin system [47], and their evolution for the manufacturer recommended cure cycle is plotted in Fig. 1. The experimentally determined cure kinetics constants for this material system, required to evaluate Eq. (2), is listed in Table 1. The evaluated degree of cure, for a specific time t, can be used to determine the material state of the thermoset as seen in Fig. 1. These properties can be used with an instantaneous linear-elastic constitutive model, previously described in Ref. [20], to predict the development of residual stresses ( $\sigma_i$ ) as a function of the evolving thermal and chemical strains as follows

$$\sigma_{i}(t) = \left[ C_{ij}(t, T, \phi) \left[ \varepsilon_{j}^{tot}(t, T, \phi) - (\varepsilon_{j}^{therm}(t, T, \phi) + \varepsilon_{j}^{shrink}(t, T, \phi)) \delta_{j} \right] \right],$$

$$where \ \delta_{j} = \begin{cases} 1 & \text{j} = 1, 2, 3\\ 0 & \text{j} > 3 \end{cases} \tag{4}$$

where  $\varepsilon_j^{tot}$ ,  $\varepsilon_j^{therm}$  and  $\varepsilon_j^{shrink}$  are respectively the total, thermal and chemical shrinkage strains, and  $C_{ij}$  is the material stiffness as a function of time, temperature, and degree of cure.

The computational approach to simulate the curing process is developed based on the instantaneous linear-elastic nature of Eq. (4). A time-based analysis, considering an incremental time period  $\Delta t$ , is performed over the cure cycle seen in Fig. 1, and the degree of cure is evaluated at each time increment. The mechanical properties of the thermoset are determined as a function of the degree of cure, based on experimental characterization data. An uncoupled displacement-temperature analysis is performed to compute the displacements and temperature fields. Finally, Eq. (4) is used to predict the residual stress developed within the thermoset material.

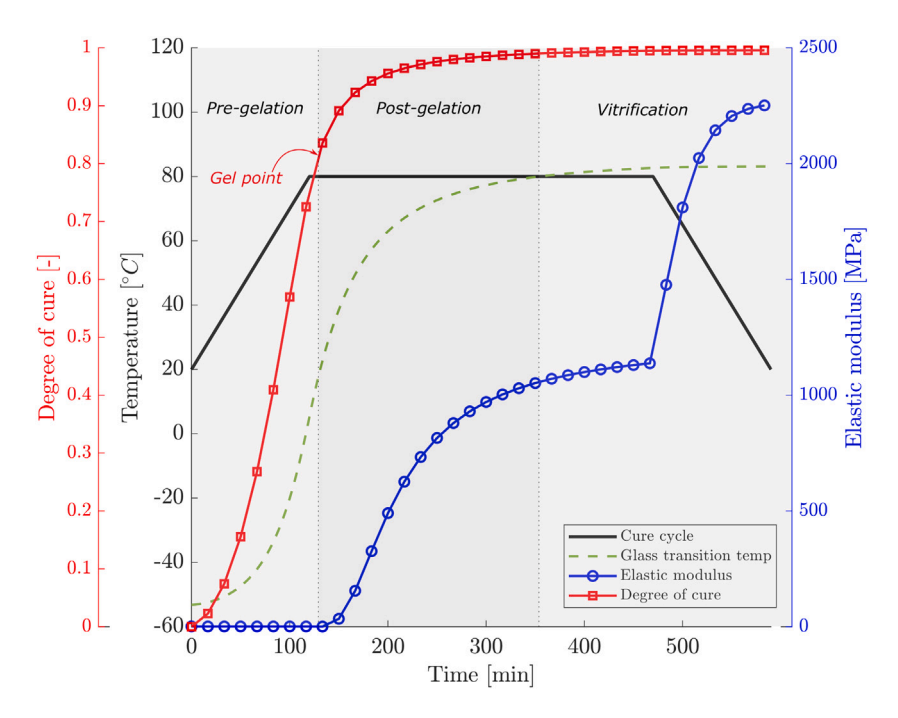


Fig. 1. Temperature - degree of cure plot of RIM R135/H1366 epoxy resin system with evolution of the elastic modulus.

Table 1
Cure kinetics parameters for the RIM R135/H1366 enovy resin system [47]

cpoxy resin system [ 17 ].	
Cure kinetic parameter	Value
Exponent m	0.4 [-]
Exponent n	1.5 [-]
Rate constant $A_1$	$3.6 \times 10^9 \text{ [s}^{-1}\text{]}$
Rate constant $A_2$	$0.01245 [s^{-1}]$
Activation energy $\Delta E_1$	85.3 [kJ/mol]
Activation energy $\Delta E_2$	11.1 [kJ/mol]

# 2.2. Higher-order FE formulation

The Carrera Unified Formulation (CUF) is a generalized framework to derive higher-order structural theories, and in combination with the Finite Element Method (FEM), can be used to develop higher-order numerical models. Specifically, CUF allows for the kinematic enrichment of beam (1D-CUF) and plate/shell (2D-CUF) elements by the use of additional interpolation functions, resulting in numerical models that approach the accuracy of 3D-FEA at significantly reduced computational effort [38].

The current work uses 1D-CUF models, wherein the cross-section of beam elements is explicitly defined by a set of additional interpolation functions, termed as expansion functions ( $F_{\rm r}$ ). This modeling approach enables composite modeling across various characteristic length-scales, and is schematically shown in Fig. 2. Within 1D-CUF, the displacement field is defined as [38]

$$\mathbf{u} = F_{\tau}(x, z)\mathbf{u}_{\tau}(y), \ \tau = 1, 2, \dots, M$$
(5)

where M is the number of terms within the expansion function. Various classes of polynomial functions can be used as  $(F_\tau)$ , and is chosen by the user. The most popular choice of expansion function are those based on Taylor series [48] and Lagrange polynomials [49]. Various other functions have been proposed to enhance the cross-sectional interpolation [50,51]. The present work considers the use of Lagrange polynomials as  $F_\tau$ , which consist of nodal interpolation functions within the cross-sectional discretization, see Fig. 2. This leads to a purely

displacement-based formulation as seen below:

$$u^{x} = \sum_{i=1}^{N node} F_{i}(x, z) \cdot u_{i}^{x}$$

$$u^{y} = \sum_{i=1}^{N node} F_{i}(x, z) \cdot u_{i}^{y}$$

$$u^{z} = \sum_{i=1}^{N node} F_{i}(x, z) \cdot u_{i}^{z}$$
(6)

where  $u_i^x$ ,  $u_i^y$ ,  $u_i^z$  and  $F_i(x,z)$  are the translational degrees of freedom (DOF) and the interpolation function, respectively, of node *i*. Furthermore, the use of cross-sectional Lagrange elements allows for the explicit modeling of each component domain within the structure, and is known as Component-Wise modeling [52.53].

The stress and strain fields are defined using the Voigt notation as follows:

$$\sigma = \{\sigma_{xx}, \sigma_{yy}, \sigma_{zz}, \sigma_{xy}, \sigma_{xz}, \sigma_{yz}\} 
\varepsilon = \{\varepsilon_{xx}, \varepsilon_{yy}, \varepsilon_{zz}, \varepsilon_{xy}, \varepsilon_{xz}, \varepsilon_{yz}\}$$
(7)

Considering infinitesimal strain theory, the displacement–strain relationship is described using the differential operator  ${\bf D}$  as

$$\varepsilon = Du$$
 (8)

with

$$\mathbf{D} = \begin{bmatrix} \frac{\partial}{\partial x} & 0 & 0\\ 0 & \frac{\partial}{\partial y} & 0\\ 0 & 0 & \frac{\partial}{\partial z}\\ \frac{\partial}{\partial y} & \frac{\partial}{\partial x} & 0\\ \frac{\partial}{\partial z} & 0 & \frac{\partial}{\partial x}\\ 0 & \frac{\partial}{\partial z} & \frac{\partial}{\partial z} \end{bmatrix}$$

The stress-strain relation is given as

$$\sigma = \mathbf{C}(t, T, \phi)\varepsilon \tag{9}$$

where C is the  $6\times 6$  material stiffness matrix. In the present work, C depends on the ongoing cure state which is defined by the time, temperature, and degree of cure as described in Section 2.1. Discretizing the

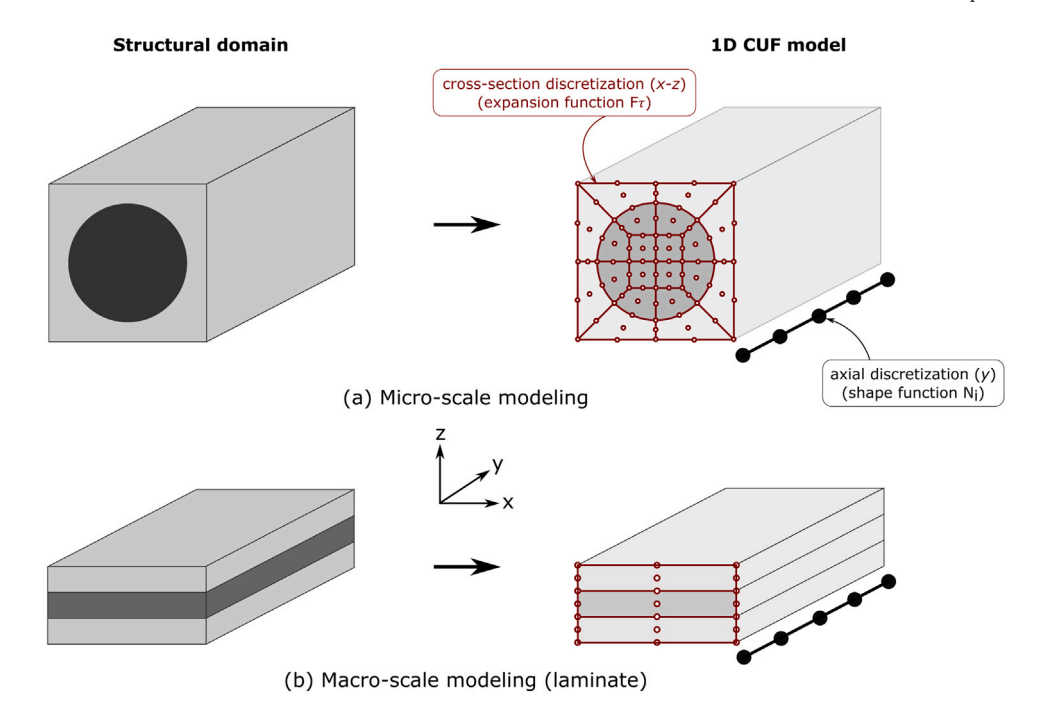


Fig. 2. Composite modeling using 1D CUF. (a) Micro-scale CUF model, and (b) Macro-scale (laminate-level) CUF model.

structure, schematically shown in Fig. 2, along its axis with 1D finite elements (using interpolation functions  $N_i$ ), and refining the cross-sectional kinematics using expansion functions  $F_\tau$ , the 3D displacement can be written as

$$\mathbf{u}(x, y, z) = F_{\tau}(x, z)N_{i}(y)\mathbf{u}_{\tau i}$$
(10)

According to the principle of virtual work

$$\delta L_{int} = \delta L_{ext} \tag{11}$$

where the virtual variation of the internal strain energy  $\delta L_{int}$  is defined as

$$\delta L_{int} = \int_{V} \delta \boldsymbol{\epsilon}^{T} : \boldsymbol{\sigma} \tag{12}$$

Combining Eqs. (9), (10) and (12), the stiffness matrix can be derived as

$$\delta L_{int} = \delta \mathbf{u}_{sj}^T \mathbf{k}_{ij\tau s} \mathbf{u}_{\tau i} \tag{13}$$

with

$$\mathbf{k}_{ij\tau s} = \int_{I} \int_{A} \mathbf{D}^{T}(N_{i}(y)F_{\tau}(x,z))\mathbf{C}(t,T,\phi)\mathbf{D}(N_{j}(y)F_{s}(x,z)) \ dA \ dl$$
 (14)

The 3  $\times$  3 matrix  $\mathbf{k}_{ij\tau s}$  is the Fundamental Nucleus (FN), and its definition remains invariant with respect to any given combination of interpolation function  $N_i$  and expansion function  $F_{\tau}$ . The element-level stiffness matrix can then be computed by assembling the fundamental nuclei associated with each combination of the nodal indices  $\{i, j, \tau, s\}$ . The numerical model used in the current work requires a temperature DOF, in addition to the three mechanical DOF, in order to simulate the thermoset curing process. The temperature DOF can be accounted for in the FN by considering a thermal term  $k_{\theta}$  as follows [54]

$$k_{\theta} = \int_{I} \int_{A} \nabla^{T} (N_{i} F_{\tau}) \kappa \nabla (N_{j} F_{s}) \, dA \, dl \tag{15}$$

where  $\kappa$  is the material thermal conductivity. Considering an uncoupled temperature–displacement problem, the augmented FN is now a 4  $\times$  4 matrix, defined as

$$k_{ij\tau s}^{u\theta} = \begin{bmatrix} \mathbf{k}_{ij\tau s} & \mathbf{0} \\ \mathbf{0} & \mathbf{k}_{\theta} \end{bmatrix} \tag{16}$$

#### 3. Experimental validation at the macro-scale

Experimental tests were conducted at the macro-scale to validate the proposed process modeling framework by comparing the predicted and measured warpage in anti-symmetric laminates as a consequence of the manufacturing process. A  $[0_2/90_2]$  cross-ply laminate, composed of IM7 fiber and RIM R135/H1366 epoxy resin, was fabricated and its curing-induced warpage was measured using imaging techniques. A detailed description of the fabrication and imaging procedures is provided hereinafter.

# 3.1. Laminate fabrication

A  $[0_2/90_2]$  cross-ply laminate was fabricated to validate the present process modeling framework. A hand lamination technique was used for the fabrication of the panel. Four plies of unidirectional IM7 carbon fibers (supplied by Fiber Glast) were cut into 6-inch × 6-inch squares. These plies were stacked in a  $[0_2/90_2]$  configuration. A thin coat of RIM R135/H166 resin (supplied by Westlake Epoxy) mixture was applied between each ply, to ensure wetting of the plies and to avoid any dry spots. A final coat of epoxy was applied to the top ply after the plies were stacked according to the specified sequence. The laminate was assembled on a glass plate between two sheets of PTFE (polytetrafluoroethylene - supplied by Fiber Glast) to prevent any adhesion between the bottom surface of the laminate and glass plate, and between the top surface of the laminate and the vacuum bagging material, thereby allowing for easy demolding. The assembled laminate was sealed inside a vacuum bag with a small outlet for the vacuum pump connection. The fabrication setup is shown in Fig. 3. The vacuum-sealed laminate was left at room temperature for 20 min to ensure a tight seal. During this period, a hand roller was passed over the plies to squeeze out any excess resin. At the end of the 20 min, the laminate assembly was transferred into an oven which was programmed to run the temperature profile shown in Fig. 1. The prescribed cure cycle ensured a full cure of the epoxy resin. Subsequently, the fabricated part was de-molded and the developed cure-induced deformation was measured.

# 3.2. Warpage measurement via 3D-DIC

3D Digital Image Correlation (3D-DIC) was used to measure the geometry profile of the fabricated cross-ply laminate. To perform 3D-

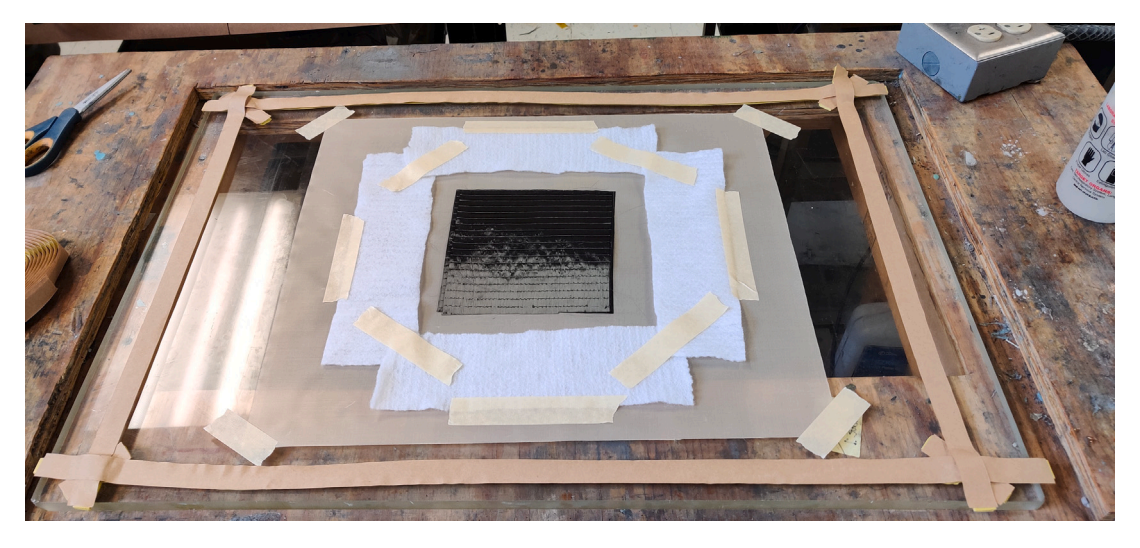


Fig. 3.  $[0_2/90_2]$  cross-ply laminate fabrication setup.

Table 2
Setup parameters used for the 3D-DIC analysis.

Calibration		Facets		Filtering	
Deviation [Pixel]	0.032	Size [Pixel]	30 × 30	Type [-]	Median
Scale deviation [mm]	0.001	Step [Pixel]	$27 \times 27$	Run [-]	5
Intersection [Pixel]	0.500	Mode [-].	Rectangular	Size [-]	3

DIC measurements, a stochastic pattern (e.g. black dots on a white background) is applied to the surface of interest and the relative position of groups of pixel (i.e., facet) is tracked as the surface deforms over time [55]. Before performing 3D-DIC measurements, the position of the cameras relative to each other and the distortions of the individual lenses must be determined through a calibration process [56]. In the present work, this operation was performed using a National Institute of Standard and Technology (NIST)-coded calibration panel.

The stereovision system selected for performing the tests consisted of a pair of 12 Megapixel monochrome Toshiba Teli CSC12M25BMP19-01B CleverDragon cameras that use a complementary metal oxide semiconductor (CMOS) image sensor with a 6  $\mu m$  square pixel size and a resolution of 4096 x 3072 pixels. The cameras were fitted with two 24 mm focal length lenses. The stereovision system was positioned to have a working distance of 0.35 m from the surface of the specimen, a camera base distance of 0.18 m, and a cameras' separation angle of 26.8°. Two LED lights were used to illuminate the specimen surface.

The tests were performed to characterize the geometrical profile of the cross-ply laminate. Ten images were taken to allow data averaging during post-processing, and obtain more accurate information. The acquired images were processed using the software ARAMIS by GOM. The setup parameters used in the analysis are summarized in Table 2.

# 3.3. Macro-scale process simulation and validation

The structural modeling approach described in Section 2.2 is employed in composite process modeling at the macroscopic length-scale, and enables the prediction of structural distortions after the curing and tool removal process. The cure kinetics model (see Section 2.1) is used to evaluate the resin cure state, and hence the evolving material properties, based on the applied cure cycle. The effective ply properties are then obtained by homogenization, via the ply micromechanics model by Bogetti and Gillespie [57]. Both the composite part and the mold are explicitly modeled in the process simulation to account for the effect of tool removal. A shear layer, i.e., a layer of elements with reduced shear stiffness, is used to represent the tool/part interface and allow for frictionless interaction between the tool and part [46]. At the end of the cure cycle, an additional mechanical analysis is performed to simulate

the tool removal procedure and predict the final composite deformed shape after demolding [58]. The following provides an overview of the tool removal process, and is summarized as a flowchart in Fig. 4:

Considering an increment n within the time-based process analysis, corresponding to time  $t_n$ , the mechanical problem is described as [46]

$$\mathbf{K}_n \Delta \mathbf{U}_n = \Delta \mathbf{F}_n \tag{17}$$

where  $\mathbf{K}_n$  is the global stiffness matrix including contributions from the tool, composite part, and the shear layer.  $\Delta \mathbf{U}_n$  is the incremental displacement as a result of the incremental thermal and shrinkage strains represented by  $\Delta \mathbf{F}_n$ . The interfacial force term representing the constraint of the tool on the part can be calculated as

$$\Delta \mathbf{F}_{n}^{interface} = \mathbf{K}_{n}^{part} \Delta \mathbf{U}_{n}^{part} - \Delta \mathbf{F}_{n}^{part}$$
(18)

where the quantities with superscript 'part' refers to components containing degrees of freedom associated with only the composite part. The incremental force terms calculated from Eq. (18) at each time-step are summed at the end of the cure analysis to obtain the total interfacial forces acting on the part as follows

$$\mathbf{F}^{interface} = \sum_{n=1}^{N_{steps}} \Delta \mathbf{F}_{n}^{interface} \tag{19}$$

The deformation  $U^*$  due to the total interface force evaluated in Eq. (19) is computed by solving the following problem

$$\mathbf{K}^{part}\mathbf{U}^* = \mathbf{F}^{interface} \tag{20}$$

The final deformed state of the composite structure, after curing and tool-removal, is obtained as

$$\mathbf{U}^{part} = \mathbf{U}^* + \sum_{n=1}^{N_{steps}} \Delta \mathbf{U}_n^{part} \tag{21}$$

Laminate-level process modeling is performed to predict the cure-induced warpage of a IM7/RIM R135-H1366  $[0_2/90_2]$  cross-ply laminate, and compared to the experimentally obtained deformation data of the fabricated composite panel (see Section 3.1). The analysis geometry and the corresponding CUF model, including both the tool and the composite laminate, are shown schematically in Fig. 5. The material

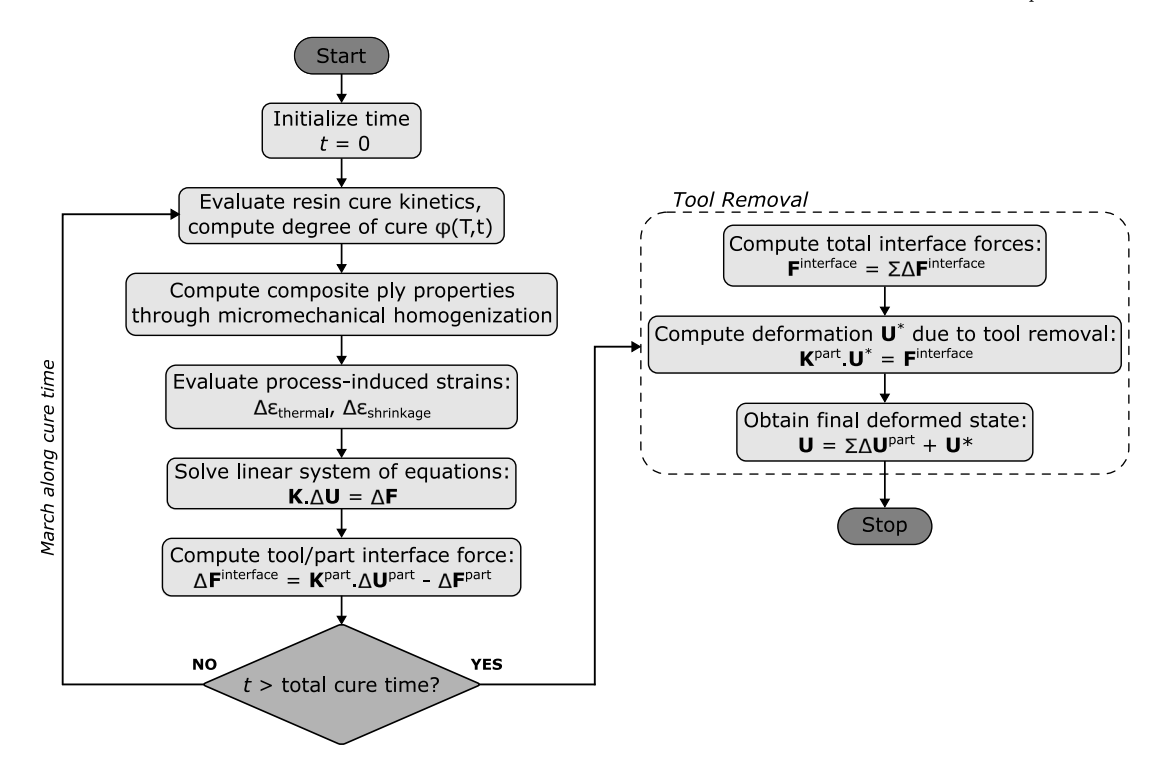


Fig. 4. Flowchart of the macro-scale process simulation analysis.

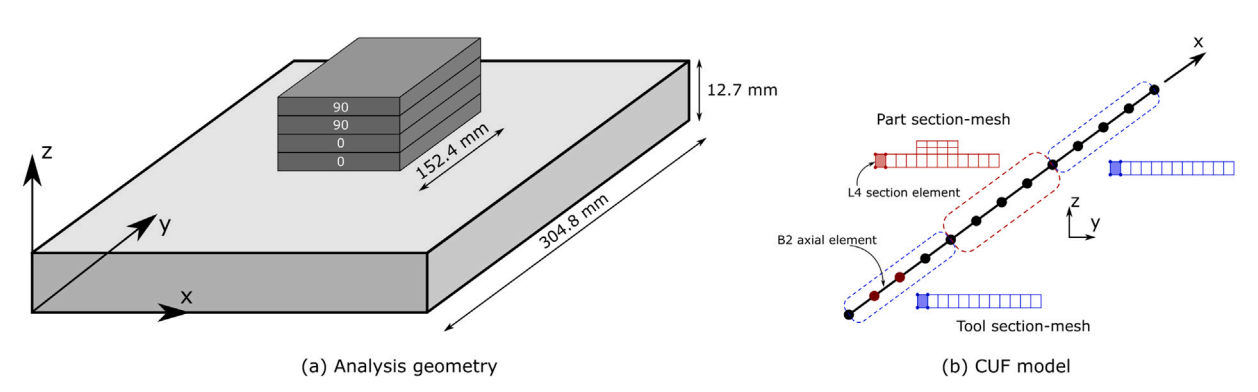


Fig. 5. (a) Schematic representation of the [0,90,] cross-ply laminate with tool, (b) CUF model used in the macro-scale process analysis.

properties of IM7 fiber and RIM R135-H1366 epoxy resin are listed in Table 3 and Table 4, respectively. The tool has been modeled as an isotropic elastic material with a Young's modulus of 75 GPa and a Poisson's ratio of 0.3. The entire geometry is modeled along the *x*-axis using 12 B2 elements. The composite laminate section is discretized with 16 L4 elements, and is based on a convergence study. Plies with the same fiber orientation have been modeled using a single section element in the thickness direction (*z*-axis). During the curing process, the bottom surface of the tool is fully constrained, and a temperature boundary condition is prescribed according to the cure cycle shown in Fig. 1. Symmetry conditions are applied on the composite part during the tool removal procedure.

The described CUF model is used to perform the curing simulation, and subsequently, the tool removal step to evaluate the final warped profile of the laminate. The vertical deflection  $(u_z)$  distribution of the laminate is visualized as a contour plot in Fig. 6. Also shown is the fabricated cross-ply laminate in its post-cure warped configuration. The predicted CUF warpage is compared with the experimentally measured deflection, as summarized in Table 5. It is seen that the numerically predicted maximum warpage of 0.53 mm is in very good agreement with the experimentally measured deflection of 0.488 mm (error under

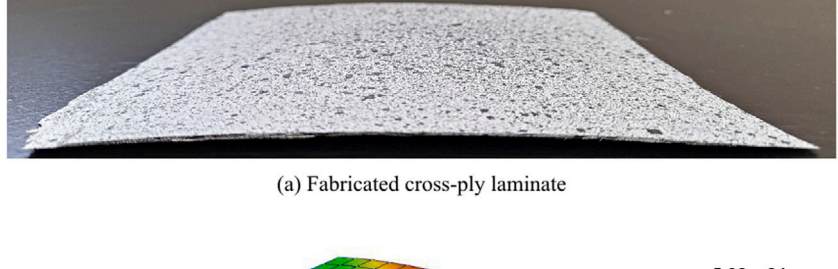
Table 3
Elastic and thermal material properties of IM7 carbon fiber [47].

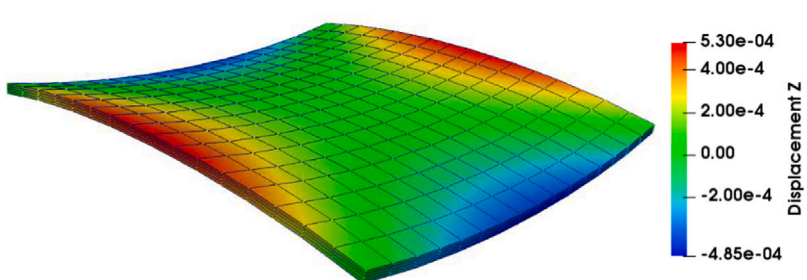
Material property	Value
Density $\rho^f$	1780.0 [kg/m <sup>3</sup> ]
Axial modulus $E_{11}^f$	276.0 [GPa]
Transverse modulus $E_{22}^f$ , $E_{33}^f$	19.5 [GPa]
In-plane Poisson's ratio $v_{12}^f$ , $v_{13}^f$	0.28 [-]
Out-of-plane Poisson's ratio $v_{23}^f$	0.25 [-]
In-plane shear modulus $G_{12}^f$ , $\widetilde{G}_{13}^f$	70.0 [GPa]
Out-of-plane shear modulus $G_{23}^{73}$	7.8 [GPa]
Axial coefficient of thermal expansion (CTE) $\alpha_{11}^f$	-0.54E-6 [K <sup>-1</sup> ]
Transverse CTE $\alpha_{22}^f$ , $\alpha_{33}^f$	10.08E-6 [K <sup>-1</sup> ]
Thermal conductivity $\kappa^f$	5.4 [W/mK]
Specific heat $c_p^f$	879.0 [J/kgK]

9%), and thus provides a macro-scale validation of the proposed process modeling framework.

# 4. Process model verification at the micro-scale

A series of micro-scale numerical assessments is presented in this section, with the aim of verifying the proposed modeling approach,





(b) CUF prediction of vertical deflection u<sub>z</sub> (deformation scaled 5x)

Fig. 6. Warpage in the RIM R135/H1366 cross-ply laminate after the curing and tool-removal process. (a) Fabricated cross-ply laminate, and (b) CUF predictions of the vertical deflection  $u_z$  (unit: m).

Table 4
Elastic and thermal material properties of RIM R135/H1366 epoxy resin [47].

Material property	Value
Density $\rho^m$	1200.0 [kg/m <sup>3</sup> ]
Elastic modulus $E^m$	2482.0 [MPa]
Poisson's ratio $v^m$	0.37 [MPa]
Coefficient of thermal expansion $\alpha^m$	61.0E-6 [K <sup>-1</sup> ]
Coefficient of chemical shrinkage $\beta^m$	0.111 [-]
Thermal conductivity $\kappa^m$	0.245 [W/mK]
Specific heat $c_p^m$	1600.0 [J/kgK]

**Table 5**Comparison of numerically predicted maximum cure-induced warpage with experimental measurements for the RIM R135/H1366 cross-ply laminate.

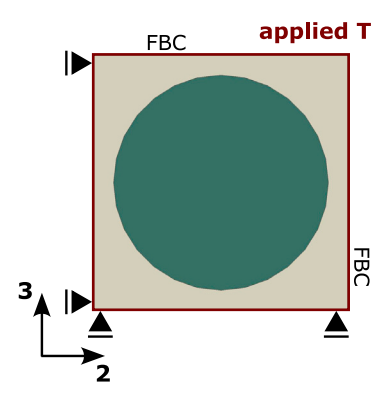
Approach	Max. deflection $u_z$ [mm]	Error [%]
Numerical (CUF)	0.530	8.6
Experimental	0.488	-

as well as to evaluate its performance with respect to conventional 3D-FEA. The reference 3D-FE analyses were performed using Abaqus/STANDARD with the kinetics model implemented using user-written subroutines [47]. The composite micromechanical models are composed of IM7 fiber and RIM R135/H1366 epoxy resin, whose thermomechanical properties were previously listed in Table 3 and 4, respectively. In each case, the cure simulation follows the cure cycle plotted in Fig. 1.

# 4.1. Curing of a square-packed RUC

The present numerical example considers the square-packed Repeating Unit Cell (RUC) with a single fiber, as shown in Fig. 7, and constitutes an initial verification of the proposed CUF process model. A prescribed temperature based on the cure cycle (See Fig. 1) is applied on the surface of the RUC. Flat Boundary Conditions (FBC), a special case of Periodic Boundary Conditions (PBC), are applied on the faces of the RUC which ensures that its faces remain flat in the deformed configuration. Further details on the use of FBC and its equivalence to PBC in the current application can be found in [20,47].

The process modeling of the square-packed RUC is performed using a series of CUF models with varying levels of refinement within the



 $\label{eq:Fig.7.} \textbf{Fig. 7.} \ \ \text{Schematic representation of a square-packed RUC with the applied boundary conditions.}$ 

Table 6
Summary of the numerical models used in the process simulation of the square-packed

No. of elements	DOF	Analysis time [s]
52 C3D8T	523	40
226 C3D8T	2,043	52
52 L4	520	3.2
227 L4	2,048	13.4
20 L9	712	4.7
52 L9	1,864	14.6
	52 C3D8T 226 C3D8T 52 L4 227 L4 20 L9	52 C3D8T 523 226 C3D8T 2,043 52 L4 520 227 L4 2,048 20 L9 712

RUC face, using both 4-node linear (L4) and 9-node quadratic (L9) quad elements. Each CUF model consists of a single linear beam element (B2) along the thickness direction. Two reference 3D-FE models are also developed in Abaqus, where the RUC thickness is represented by a single element. The discretization used in each numerical model is visualized in Fig. 8. The residual stresses in the transverse direction (22-component) that develop within the RUC at the end of the cure cycle, as predicted by the various models, is shown in the form of contour plots in Fig. 9. A summary of all the numerical models, along with the required computational time, is presented in Table 6.

From Fig. 9, it is seen that both the refined CUF and 3D-FE models are in very good agreement with each other, and provides an initial verification of the proposed numerical approach.

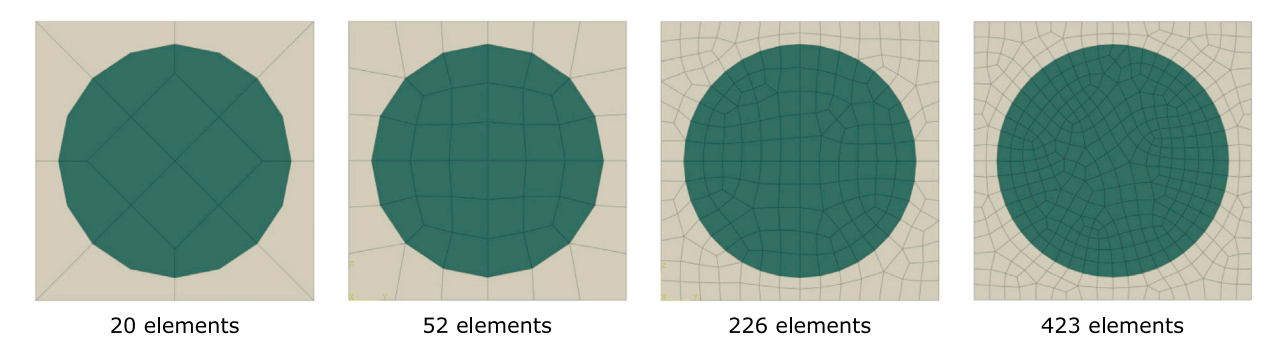


Fig. 8. Meshes used in Abaqus and CUF to discretize the square-packed RUC.

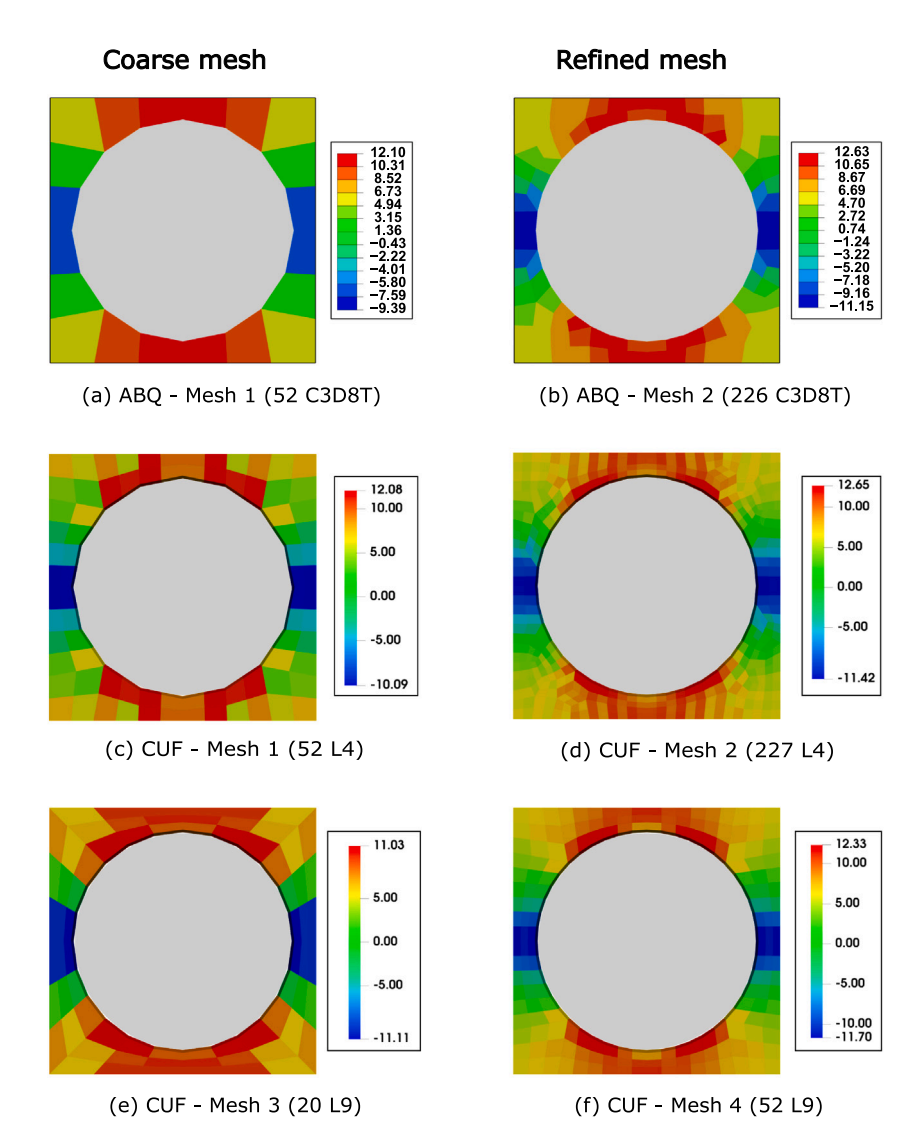


Fig. 9. Distribution of residual stress (22-component) in the square-packed RUC at the end of cure. (a,b) 3D-FE, (c,d) linear CUF, and (e,f) quadratic CUF models.

The coarser models in both cases, i.e. 'ABQ - Mesh 1' and 'CUF - Mesh 1', predict very similar stress fields, and are underestimated when compared to the refined models. A similar observation is made for the case of the 'CUF - Mesh 3' model, i.e. the coarser quadratic model, where the predicted stresses are indicative of the intermediate level of refinement within the model. It was also observed that further mesh refinement, in both CUF and 3D-FE, did lead to any significant differences thereby indicating mesh convergence. Comparing the associated computational time (see Table 6) for the refined models—'ABQ - Mesh

2' (226 C3D8T elements) with 'CUF - Mesh 2' (227 linear elements) and 'CUF - Mesh 4' (52 quadratic elements)—it is seen that the proposed CUF approach is approximately 4x as fast as the corresponding 3D-FEA, for equivalent levels of accuracy.

# 4.2. Curing of 20-fiber random RUC

This assessment considers a periodic RUC with 20 randomly distributed fibers, as shown in Fig. 10. This allows for the modeling

M.H. Nagaraj et al. Composites Part B 279 (2024) 111447

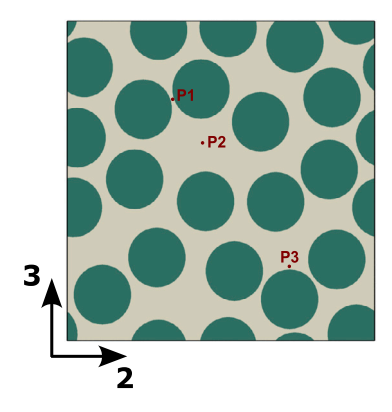


Fig. 10. RUC with 20 randomly distributed fibers.

of a realistic composite microstructure while enabling the study of fiber–matrix interactions during the curing process. The choice of the considered RUC was based on a RUC size convergence study previously reported in [47]. The RUC boundary conditions described in Section 4.1 are applied in the current analysis. A series of CUF models is developed with increasing levels of refinement within the RUC face, and a single linear beam element (B2) is used to represent the RUC thickness in each model. Three 3D-FE models are also developed in Abaqus as a numerical reference. The residual stress (22-component) predicted by the models at the end of the cure cycle is presented in Fig. 11. The residual stress evolution at three specific points – P1, P2, and P3 – within the RUC (see Fig. 10), as a function of cure time, is plotted in Fig. 12. A summary of the computational models is presented in Table 7.

From Fig. 11, it is seen that successive refinement of the mesh leads to a converged solution in both the 3D-FE and CUF models. Residual stress evolution within localized regions of the RUC, as shown in Fig. 12, is a function of resin shrinkage during cure, thermal effects, and the constraining effect of neighboring reinforcing fibers. The residual stress magnitude and state (tensile or compressive) is a cumulative effect of these factors. For instance, the presence of fibers at Points

P1 and P3 (refer Fig. 10) significantly constricts thermal expansion during the heating stage of the cure cycle and leads to an initial compressive stress state as seen in Fig. 12(a) and (c), respectively. Matrix shrinkage becomes prominent in the post-gelation stage of the curing process as sufficient polymer cross-links develop, and its arrest due to neighboring fibers leads to a net tensile stress state which reaches its peak magnitude during the thermal cooldown at the end of cure. On the other hand, Point P2 is weakly constrained due to its location at the center of a matrix-rich region. This leads to a different stress state evolution compared to Points P1 and P3, as seen in Fig. 12(b). The stress state at P2 is initially tensile during the heating stage of the cure cycle, which then becomes compressive in the post-gelation phase as matrix shrinkage gains prominence, and finally attains its maximum magnitude at the end of the cure cycle.

The coarsest models significantly underestimate the compressive stresses that develop at the point P1, which is the matrix region between two neighboring fibers, and thus a zone of considerable stress concentration within the RUC. This can be observed in Fig. 12(a), where the 'ABO - Mesh 1' and 'CUF - 678 L4' models both predict similar magnitudes of the developed residual stress, which is in strong contrast to that predicted by the more refined models. On the other hand, considering the stress evolution at the point P2, see Fig. 12(b), it is seen that all the model predictions are in good general agreement. This is attributed to the fact that the point P2 is situated in a matrixrich region, and the absence of any stress concentrator implies the sufficiency of a lower mesh density. Finally, examining the residual stress evolution at the point P3 (see Fig. 12(c)), it is seen that the coarsest 3D-FE model, i.e. 'ABQ - Mesh 1', underestimates the postcure stress magnitude, and while this is not as inaccurate as in the case of Point P1, still has a considerable error with respect to the refined models. This is explained by the fact that the Point P3 lies in the immediate vicinity of a single fiber which acts as a stress concentrator. The trends observed in the behavior of the 'ABQ - Mesh 1' model at the points P1, P2 and P3 is therefore consistent with the level of stress concentration experienced by the matrix at these points. It is noted that the corresponding coarsest CUF model, i.e. 'CUF - 678 L4', predicts a post-cure residual stress which is in good agreement with that reported by refined models, at the Point P3, inferring that the coarsest CUF model performs better than the corresponding 3D-FE model.

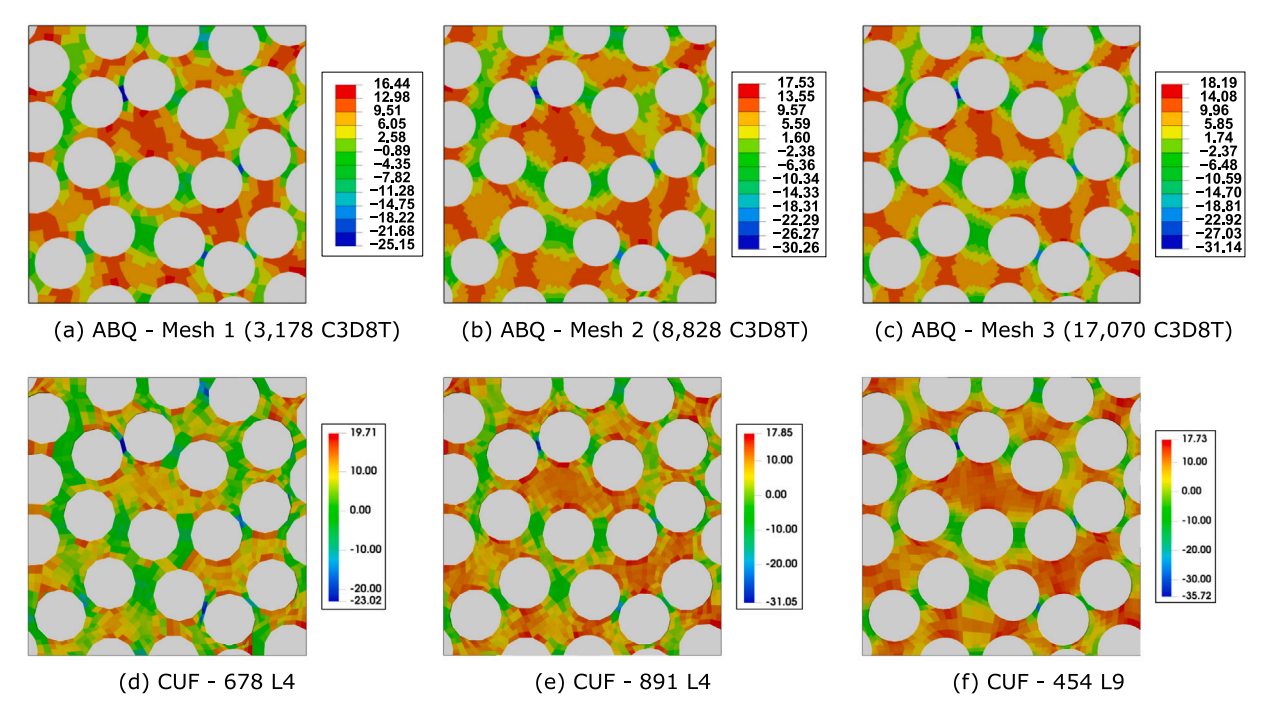


Fig. 11. Distribution of residual stress (22-component) in the 20-fiber RUC at the end of cure.

M.H. Nagaraj et al. Composites Part B 279 (2024) 111447

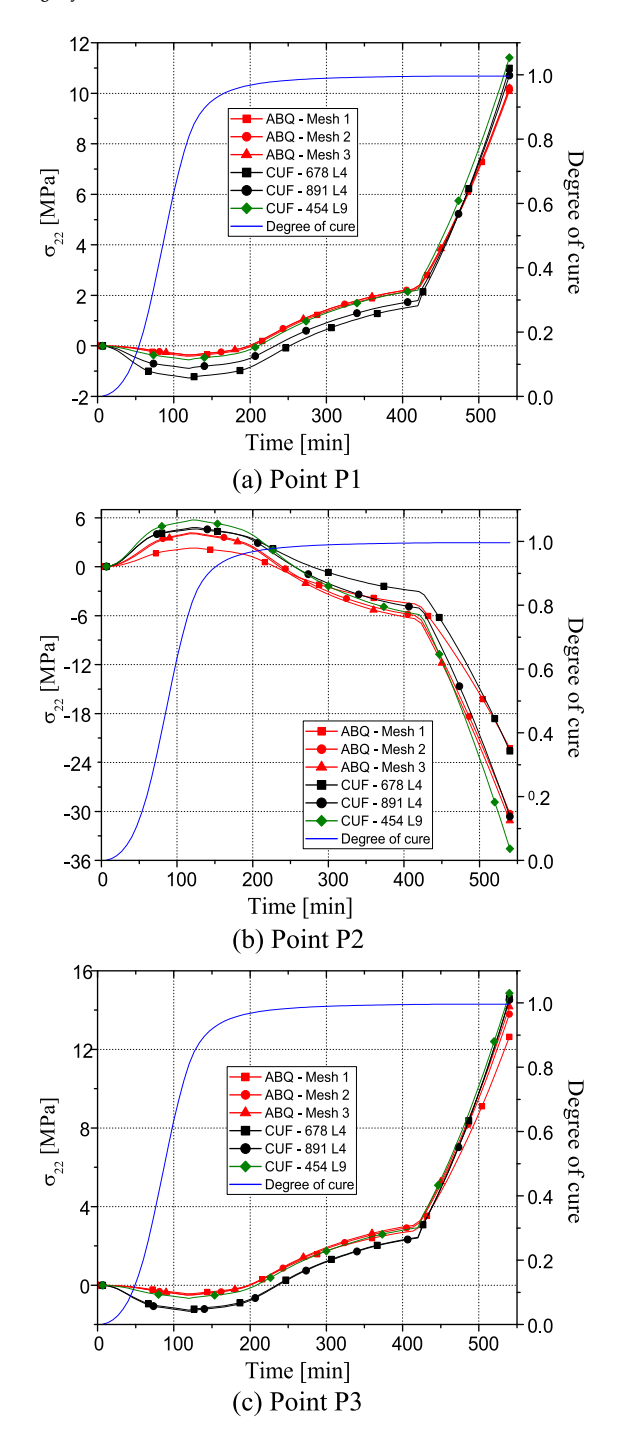


Fig. 12. Evolution of residual stress (22-component) as a function of cure time at specific points within the 20-fiber RUC.

Considering the significant variation in stress concentration at different points within the RUC, which is a consequence of the randomly distributed fibers, any numerical model would require a refined discretization of the matrix component in order to accurately predict the post-cure residual stresses. The 'ABQ - Mesh 2' model is the coarsest 3D-FE model whose results are sufficiently accurate, based on the mesh convergence study. The corresponding CUF model, with an equivalent quality of predicted results, is the 'CUF - 891 L4' model. Comparing the computational costs associated with these two models, see Table 7, it is seen that the CUF approach is approximately 10x as fast as the 3D-FE case in terms of analysis time, and is over 7x smaller in computational

Table 7
Summary of the numerical models used in the process simulation of the 20-fiber RUC.

Model	No. of elements	DOF	Analysis time [s]
Abaqus - Mesh 1	3,178 C3D8T	19,911	352
Abaqus - Mesh 2ª	8,828 C3D8T	54,447	830
Abaqus - Mesh 3	17,070 C3D8T	104,403	1622
CUF - Mesh 1	678 L4	5,728	55
CUF - Mesh 2a	891 L4	7,432	85
CUF - Mesh 3	454 L9	15,400	463

a Indicates converged results.

size based on the number of DOF within the models. An important observation is that the computational efficiency of CUF over 3D-FE, when the model domain is increased from a single-fiber RUC to a 20-fiber RUC, correspondingly increases from approximately 4x to 10x, indicating the superior scalability of CUF. Finally, the 'CUF - 454 L9' model, while very accurate, has an unnecessarily excessive level of kinematic refinement, and the corresponding higher computational cost therefore implies that a sufficiently refined L4 model (such as the 'CUF - 891 L4' model) is preferable over those based on L9, for the current class of problem. It is, however, noted that even the 'CUF - 454 L9' model is about 3.5x as fast as the most refined 3D-FE model, i.e. 'ABQ - Mesh 3', and is 6.8x smaller in size, demonstrating the computational efficiency of the CUF approach over conventional 3D-FEA.

# 5. Conclusion

A higher-order FE based process modeling framework has been proposed in the present work to investigate the influence of the manufacturing process in thermoset composites at two important length-scale resolutions: the micro- and macro-scales. Experimental validation was performed at the macro-scale by fabricating cross-ply laminated composite panels and comparing the measured and predicted cure-induced warpage. A good agreement between model and test data (error within 10%) validates the proposed process framework for thermoset composites. At the micro-scale, a series of micromechanical numerical assessments were performed for residual stress prediction during the curing process, and a verification was conducted using traditional 3D-FEA. It was shown that the proposed micromechanical process models exhibit an order-of-magnitude (~ 10x) improvement in the computational costs when compared to 3D-FEA, for equivalent accuracy of results.

The demonstrated superior performance of the higher-order FE process model therefore makes it a strong candidate for integration within multi-scale process model frameworks, leading to an accurate residual stress prediction capability that would enable the optimization of composite structures through model-based feedback on the manufacturing process.

# CRediT authorship contribution statement

M.H. Nagaraj: Writing – review & editing, Writing – original draft, Software, Methodology, Investigation, Formal analysis, Conceptualization, Data curation, Validation, Visualization, Supervision. S.P. Shah: Validation, Investigation. A. Sabato: Validation, Investigation. M. Maiaru: Writing – review & editing, Software, Resources, Project administration, Funding acquisition, Conceptualization, Supervision.

# **Declaration of competing interest**

The authors declare that they have no known competing financial interests or personal relationships that could have appeared to influence the work reported in this paper.

#### Data availability

Data will be made available upon reasonable request.

#### Acknowledgments

This material is based upon work supported by the National Science Foundation, United States CAREER Award #2145387. Any opinions, findings, and conclusions or recommendations expressed in this material are those of the author(s) and do not necessarily reflect the views of the National Science Foundation or the sponsors.

#### References

- Baran I, Cinar K, Ersoy N, Akkerman R, Hattel JH. A review on the mechanical modeling of composite manufacturing processes. Arch Comput Methods Eng 2017;24(2):365–95.
- [2] Kim KS, Hahn HT. Residual stress development during processing of graphite/epoxy composites. Compos Sci Technol 1989;36(2):121–32.
- [3] Chekanov YA, Korotkov VN, Rozenberg BA, Dhzavadyan EA, Bogdanova LM. Cure shrinkage defects in epoxy resins. Polymer 1995;36(10):2013–7.
- [4] Hu H, Cao D, Pavier M, Zhong Y, Zu L, Liu L, et al. Investigation of non-uniform gelation effects on residual stresses of thick laminates based on tailed FBG sensor. Compos Struct 2018;202:1361–72.
- [5] Fernlund G, Rahman N, Courdji R, Bresslauer M, Poursartip A, Willden K, et al. Experimental and numerical study of the effect of cure cycle, tool surface, geometry, and lay-up on the dimensional fidelity of autoclave-processed composite parts. Composites A 2002;33(3):341–51.
- [6] Fish J, Wagner GJ, Keten S. Mesoscopic and multiscale modelling in materials. Nature Mater 2021;20(6):774–86.
- [7] Yuan Z, Aitharaju V, Fish J. A coupled thermo-chemo-mechanical reduced-order multiscale model for predicting process-induced distortions, residual stresses, and strength. Internat J Numer Methods Engrg 2020;121(7):1440–55.
- [8] Yuan Z, Felder S, Reese S, Simon J-W, Fish J. A coupled thermo-chemomechanical reduced-order multiscale model for predicting residual stresses in fibre reinforced semi-crystalline polymer composites. Int J Multiscale Comput Eng. 2020;18(5)
- [9] Patil S, Shah S, Deshpande P, Kashmari K, Olaya M, Odegard G, et al. Multi-scale approach to predict cure-induced residual stresses in an epoxy system. In: Proceedings of the American society for composites thirty-fifth technical conference. 2020.
- [10] Deshpande PP, Shah S, Patil S, Kashmari K, Olaya M, Odegard GM, et al. Multiscale modelling of the cure process in thermoset polymers using ICME. In: Proceedings of the American society for composites thirty-fifth technical conference, 2020.
- [11] D'Mello RJ, Waas AM, Maiaru M, Koon R. Integrated computational modeling for efficient material and process design for composite aerospace structures. In: AIAA scitech 2020 forum. 2020, p. 0655.
- [12] Pinon Fischer OJ, Matlik JF, Schindel WD, French MO, Kabir MH, Ganguli JS, et al. Digital twin: reference model, realizations, and recommendations. Insight 2022;25(1):50-5.
- [13] Gaikwad PS, Krieg AS, Deshpande PP, Patil SU, King JA, Maiaru M, et al. Understanding the origin of the low cure shrinkage of polybenzoxazine resin by computational simulation. ACS Appl Polym Mater 2021;3(12):6407–15.
- [14] Odegard GM, Patil SU, Deshpande PP, Kanhaiya K, Winetrout JJ, Heinz H, et al. Molecular dynamics modeling of epoxy resins using the reactive interface force field. Macromolecules 2021;54(21):9815–24.
- [15] Patil SU, Shah SP, Olaya M, Deshpande PP, Maiaru M, Odegard GM. Reactive molecular dynamics simulation of epoxy for the full cross-linking process. ACS Appl Polym Mater 2021;3(11):5788–97.
- [16] Patil SU, Shah SP, Olaya M, Deshpande PP, Maiaru M, Odegard GM. Molecular dynamics study to predict thermo-mechanical properties of DGEBF/DETDA epoxy as a function of crosslinking density. 2021, arXiv preprint arXiv:2108.00933.
- [17] Odegard GM, Patil SU, Gaikwad PS, Deshpande P, Krieg AS, Shah SP, et al. Accurate predictions of thermoset resin glass transition temperatures from all-atom molecular dynamics simulation. Soft Matter 2022;18(39):7550–8.
- [18] Schey MJ, Beke T, Appel L, Zabler S, Shah S, Hu J, et al. Identification and quantification of 3D fiber clusters in fiber-reinforced composite materials. JOM
- [19] Bouaoune L, Brunet Y, El Moumen A, Kanit T, Mazouz H. Random versus periodic microstructures for elasticity of fibers reinforced composites. Composites B 2016;103:68–73.
- [20] Maiarù M, D'Mello RJ, Waas AM. Characterization of intralaminar strengths of virtually cured polymer matrix composites. Composites B 2018;149:285–95.
- [21] Shah SP, Patil SU, Hansen CJ, Odegard GM, Maiaru M. Process modeling and characterization of thermoset composites for residual stress prediction. Mech Adv Mater Struct 2021;1–12.

- [22] Shah S, Maiaru M. Microscale analysis of virtually cured polymer matrix composites accounting for uncertainty in matrix properties during manufacturing. In: Proceedings of the American society for composites thirty-third technical conference, 2018.
- [23] Maiaru M. Effect of uncertainty in matrix fracture properties on the transverse strength of fiber reinforced polymer matrix composites. In: 2018 AIAA/ASCE/AHS/aSC structures, structural dynamics, and materials conference. 2018, p. 1901.
- [24] D'Mello RJ, Waas AM. Influence of unit cell size and fiber packing on the transverse tensile response of fiber reinforced composites. Materials 2019;12(16):2565.
- [25] Pineda EJ, Bednarcyk BA, Waas AM, Arnold SM. Progressive failure of a unidirectional fiber-reinforced composite using the method of cells: Discretization objective computational results. Int J Solids Struct 2013;50(9):1203–16.
- [26] González C, LLorca J. Mechanical behavior of unidirectional fiber-reinforced polymers under transverse compression: Microscopic mechanisms and modeling. Compos Sci Technol 2007;67(13):2795–806.
- [27] Zhang S, Xu Y, Zhang W. A novel micromechanical model to study the influence of cure process on the in-plane tensile properties of z-pinned laminates. Compos Struct 2022;300:116156.
- [28] Herráez M, González C, Lopes CS, De Villoria RG, LLorca J, Varela T, et al. Computational micromechanics evaluation of the effect of fibre shape on the transverse strength of unidirectional composites: an approach to virtual materials design. Composites A 2016;91:484–92.
- [29] Kosztowny CJR, Waas AM. Postbuckling response of unitized stiffened textile composite panels: Experiments. Int J Non-Linear Mech 2021;137:103814.
- [30] D'Mello RJ, Waas AM. Virtual curing of textile polymer matrix composites. Compos Struct 2017;178:455–66.
- [31] Okereke MI, Akpoyomare AI, Bingley MS. Virtual testing of advanced composites, cellular materials and biomaterials: a review. Composites B 2014;60:637–62.
- [32] O'Brien DJ, Mather PT, White SR. Viscoelastic properties of an epoxy resin during cure. J Compos Mater 2001;35(10):883–904.
- [33] Kenny JM. Determination of autocatalytic kinetic model parameters describing thermoset cure. J Appl Polym Sci 1994;51(4):761–4.
- [34] Yousefi A, Lafleur PG, Gauvin R. Kinetic studies of thermoset cure reactions: a review. Polym Compos 1997;18(2):157–68.
- [35] Kamal MR, Sourour S. Kinetics and thermal characterization of thermoset cure. Polym Eng Sci 1973;13(1):59–64.
- [36] Ding A, Li S, Wang J, Zu L. A three-dimensional thermo-viscoelastic analysis of process-induced residual stress in composite laminates. Compos Struct 2015;129:60–9.
- [37] Hui X, Xu Y, Wang J, Zhang W. Microscale viscoplastic analysis of unidirectional CFRP composites under the influence of curing process. Compos Struct 2021;266:113786.
- [38] Carrera E, Cinefra M, Petrolo M, Zappino E. Finite element analysis of structures through unified formulation. John Wiley & Sons; 2014.
- [39] Nagaraj MH, Reiner J, Vaziri R, Carrera E, Petrolo M. Progressive damage analysis of composite structures using higher-order layer-wise elements. Composites B 2020;190:107921.
- [40] Nagaraj MH, Reiner J, Vaziri R, Carrera E, Petrolo M. Compressive damage modeling of fiber-reinforced composite laminates using 2D higher-order layer-wise models. Composites B 2021;215:108753.
- [41] Nagaraj MH, Carrera E, Petrolo M. Progressive damage analysis of composite laminates subjected to low-velocity impact using 2D layer-wise structural models. Int J Non-Linear Mech 2020;127:103591.
- [42] Kaleel I, Petrolo M, Waas AM, Carrera E. Computationally efficient, high-fidelity micromechanics framework using refined 1D models. Compos Struct 2017;181:358–67.
- [43] Maiarú M, Petrolo M, Carrera E. Evaluation of energy and failure parameters in composite structures via a component-wise approach. Composites B 2017;108:53–64.
- [44] Carrera E, Petrolo M, Nagaraj MH, Delicata M. Evaluation of the influence of voids on 3D representative volume elements of fiber-reinforced polymer composites using CUF micromechanics. Compos Struct 2020;254:112833.
- [45] Nagaraj MH, Maiaru M. A novel higher-order finite element framework for the process modeling of material extrusion additive manufacturing. Addit Manuf 2023;76:103759.
- [46] Zappino E, Zobeiry N, Petrolo M, Vaziri R, Carrera E, Poursartip A. Analysis of process-induced deformations and residual stresses in curved composite parts considering transverse shear stress and thickness stretching. Compos Struct 2020;241:112057.
- [47] Shah SP, Maiarù M. Effect of manufacturing on the transverse response of polymer matrix composites. Polymers 2021;13(15):2491.
- [48] Carrera E, Giunta G. Refined beam theories based on a unified formulation. Int J Appl Mech 2010;2(01):117–43.
- [49] Carrera E, Petrolo M. Refined beam elements with only displacement variables and plate/shell capabilities. Meccanica 2012;47(3):537-56.
- [50] Zappino E, Li G, Pagani A, Carrera E, de Miguel AG. Use of higher-order Legendre polynomials for multilayered plate elements with node-dependent kinematics. Compos Struct 2018;202:222–32.

- [51] Carrera E, Filippi M, Zappino E. Laminated beam analysis by polynomial, trigonometric, exponential and zig-zag theories. Eur J Mech A Solids 2013:41:58–69.
- [52] Carrera E, Maiarú M, Petrolo M. Component-wise analysis of laminated anisotropic composites. Int J Solids Struct 2012;49(13):1839–51.
- [53] Carrera E, Maiaru M, Petrolo M, Giunta G. A refined 1D element for the structural analysis of single and multiple fiber/matrix cells. Compos Struct 2013;96:455–68.
- [54] Entezari A, Filippi M, Carrera E. Unified finite element approach for generalized coupled thermoelastic analysis of 3D beam-type structures, part 1: Equations and formulation. J Therm Stresses 2017;40(11):1386–401.
- [55] Sutton MA, Orteu JJ, Schreier H. Image correlation for shape, motion and deformation measurements: basic concepts, theory and applications. Springer Science & Business Media; 2009.
- [56] Bottalico F, Niezrecki C, Jerath K, Luo Y, Sabato A. Sensor-based calibration of camera's extrinsic parameters for stereophotogrammetry. IEEE Sens J 2023;23(7):7776–85.
- [57] Bogetti TA, Gillespie Jr JW. Process-induced stress and deformation in thicksection thermoset composite laminates. J Compos Mater 1992;26(5):626–60.
- [58] Johnston A, Vaziri R, Poursartip A. A plane strain model for processinduced deformation of laminated composite structures. J Compos Mater 2001;35(16):1435–69.